

See discussions, stats, and author profiles for this publication at: <https://www.researchgate.net/publication/283243946>

# A facile hydrothermal synthesis of MnO<sub>2</sub> nanorod–reduced graphene oxide nanocomposites possessing excellent microwave absorption properties

Article in RSC Advances · October 2015

DOI: 10.1039/C5RA15165A

CITATIONS

81

READS

1,321

4 authors, including:



Hongtao Guan  
Yunnan University

69 PUBLICATIONS 1,693 CITATIONS

[SEE PROFILE](#)



Shangfeng Du  
University of Birmingham

74 PUBLICATIONS 2,001 CITATIONS

[SEE PROFILE](#)



Yude Wang  
Yunnan University

227 PUBLICATIONS 7,542 CITATIONS

[SEE PROFILE](#)

Some of the authors of this publication are also working on these related projects:



MnO<sub>2</sub> nanostructures for microwave absorbing applications [View project](#)



AP thermal decomposition [View project](#)



CrossMark  
 click for updates

Cite this: *RSC Adv.*, 2015, 5, 88979

# A facile hydrothermal synthesis of MnO<sub>2</sub> nanorod-reduced graphene oxide nanocomposites possessing excellent microwave absorption properties†

Yan Wang,<sup>a</sup> Hongtao Guan,<sup>a</sup> Shangfeng Du<sup>\*b</sup> and Yude Wang<sup>\*ac</sup>

Pure MnO<sub>2</sub> nanorods and MnO<sub>2</sub> nanorod/reduced graphene oxide (RGO) nanocomposites are prepared for microwave absorption by using a simple one-step hydrothermal method without using any toxic solvents. The results demonstrate that the MnO<sub>2</sub> phases possess a high crystallization degree in both the pure nanorods and the nanocomposites but the nanocomposites exhibit two hybrid Mn phases, distinct from MnO<sub>2</sub> in the pure nanorods. The electromagnetic characteristics and electromagnetic wave (EMW) absorption properties of the materials are investigated. The thickness dependent reflection loss shows that the peak frequency and effective absorption bandwidth all decrease with the increasing material thickness. Compared with the pure MnO<sub>2</sub> nanorods, the introduction of RGO enhances the microwave absorbing intensity and effective absorption bandwidth. The maximum reflection loss value of the nanocomposites reaches  $-37$  dB at 16.8 GHz with a thickness of 2.0 mm and the wide bandwidth corresponding to the reflection loss below  $-10$  dB starts from 13 GHz until a value of  $-22$  dB at 18 GHz. The enhanced microwave absorbing properties can be ascribed to the improved permittivity, dielectric loss and especially the synergistic effects between MnO<sub>2</sub> nanorods and RGO nanosheets at their interfaces in the unique nanostructures of the MnO<sub>2</sub>/RGO nanocomposites.

Received 30th July 2015  
 Accepted 15th October 2015

DOI: 10.1039/c5ra15165a

[www.rsc.org/advances](http://www.rsc.org/advances)

## 1. Introduction

With the development of electronic and communication technology, electromagnetic interference (EMI) or signal interference has become one of the emerging issues in air pollution, water contamination and noise pollution. As a result, the utilization of materials with electromagnetic (EM) absorption properties has attracted great attention because of their high activity in shielding and diminishing interference signals to maintain the normal operation of electronic devices.<sup>1–8</sup> Furthermore, electromagnetic wave absorbing materials, also known as stealth materials, have also aroused considerable attention in the scientific community, civil, commercial and military fields due to their excellent capability in microwave attenuation, screening and absorption in the microwave band range.<sup>9–12</sup> To meet the requirements for the purpose of

microwave attenuation and certain communication, appropriate electrical conductivities and excellent dielectric or magnetic loss properties are required for a good electromagnetic wave (EMW) absorbent.<sup>13</sup> However, how to design electromagnetic absorbing materials with light weight, excellent absorption ability and wide effective absorption frequency band at a proper thickness still remains a challenge.

Carbon nanomaterials possess high-efficiency EM wave attenuation property because of their thermally activated carrier hopping associated with defect states, which means the defect state making the carbon nanomaterials lying in an unstable state of thermodynamic and providing the activation energy for the hopping of carrier which is in favor of improving the EM wave attenuation property,<sup>14</sup> their light weight, good resistance against corrosion and high conductivity.<sup>15</sup> As a representative of novel carbon nanomaterials, reduced graphene oxide (RGO) possess many unique attributes due to its extremely high specific surface areas, thermal conductivity, mechanical properties and carrier mobilities coupled with abundant surface defects and functional groups, which make it to be a promising candidate for high loss tangent and high efficiency EMI shielding applications.<sup>16,17</sup> Recently, considerable efforts have been made towards the development of RGO-based composites for microwave absorption materials, and excellent performance was also demonstrated. Zhang *et al.* synthesized RGO/ $\alpha$ -Fe<sub>2</sub>O<sub>3</sub>

<sup>a</sup>Department of Materials Science and Engineering, Yunnan University, 650091 Kunming, People's Republic of China. E-mail: ydawang@ynu.edu.cn; Fax: +86-871-65153832; Tel: +86-871-65031124

<sup>b</sup>School of Chemical Engineering, University of Birmingham, Edgbaston, Birmingham B15 2TT, UK. E-mail: s.du@bham.ac.uk

<sup>c</sup>Yunnan Province Key Lab of Micro-Nano Materials and Technology, Yunnan University, 650091 Kunming, People's Republic of China

† Electronic supplementary information (ESI) available. See DOI: 10.1039/c5ra15165a

composite hydrogel and its maximum absorption reached  $-33.5$  dB at  $7.12$  GHz with a thickness of  $5$  mm, and the product with a thickness of  $3.0$  mm showed a bandwidth of  $6.4$  GHz (from a frequency of  $10.8$ – $17.2$  GHz) corresponding to reflection loss below  $-10$  dB.<sup>18</sup> Zong *et al.* fabricated RGO-Fe<sub>3</sub>O<sub>4</sub> composites by a co-precipitation route. The maximum reflection loss of the composites reached  $-44.6$  dB at  $6.6$  GHz with a thickness of  $3.9$  mm, but the bandwidth of reflection less than  $-10$  dB was only  $2.0$  GHz (from  $5.7$  to  $7.7$  GHz).<sup>19</sup> Zhang *et al.* prepared RGO-MnFe<sub>2</sub>O<sub>4</sub> nanocomposites through a two-step method under ultrasonic treatment and the maximum reflection loss reached  $-29.0$  dB at  $9.2$  GHz, and the bandwidth of frequency less than  $-10$  dB was from  $8.00$  to  $12.88$  GHz.<sup>20</sup>

As one of the most attractive inorganic materials, manganese dioxide has been extensively applied as catalysts,<sup>21</sup> molecular sieves<sup>22</sup> and battery materials<sup>23</sup> due to its outstanding properties of ion exchange, molecular absorption, catalytic, electrochemical and magnetic performances, as well as its low cost and environmentally friendly nature. However, pure manganese dioxide obtained cannot meet the required standards of microwave absorbents and several attempts have been made to prepare doped manganese dioxide compounds for microwave absorbing characteristics. Such as, Duan *et al.* fabricated Fe-doped MnO<sub>2</sub> with a hollow sea urchin-like ball chain shape, under a higher magnetic field of  $10$  T, but the product only showed a maximum reflection loss of  $-1.02$  dB at  $18$  GHz.<sup>24</sup> By a facile water-bathing precipitation, our group synthesized Ni-doped  $\alpha$ -MnO<sub>2</sub> with much improved microwave absorbing performance. The absorption peak value reached  $-26.8$  dB and an (reflection loss exceeding  $-10$  dB) of  $3.7$  GHz ( $14.3$ – $18$  GHz) with a thickness of  $2$  mm was achieved.<sup>25</sup> Even Wang *et al.* has reported the maximum reflection loss of MnO<sub>2</sub> nanoparticles-graphene composite with a thickness of  $2.0$  mm being only  $-20.9$  dB (ref. 26) and Gupta *et al.* has explored the EMI shielding effectiveness in the frequency of Ku band of MnO<sub>2</sub> decorated graphene nanoribbons with the maximum shielding of  $-57$  dB,<sup>44</sup> which is quite different from the performance of electromagnetic and the fabrication of our materials. Nowadays, there are a few reports about the microwave absorption performance of MnO<sub>2</sub> nanorods-RGO nanocomposite.

In this work, we demonstrate that the excellent permittivity and EMW absorbing characteristics can be achieved by MnO<sub>2</sub> nanorods/RGO composite. The composite is synthesized by using a simple one-step hydrothermal method and the microwave absorption properties are investigated at frequency ranging from  $2$  to  $18$  GHz and compared with the as-prepared pure MnO<sub>2</sub> nanorods. The result clearly indicates that the introducing of RGO has a great influence on the microwave absorption performance of the composite and the very specific mechanisms on the enhanced EM absorption behavior are investigated thoroughly.

## 2. Experimental

### 2.1 Materials

All chemicals were analytical grade and used as obtained without further purification.

Natural flake graphite with purity  $99.95\%$  and BS mesh  $500$  was purchased from Chongyang Graphite Co. Ltd., Qingdao, China. KMnO<sub>4</sub> (purity no less than  $99.5\%$ ) was purchased from Dahao Fine Chemicals Co. Ltd., Shantou, China. NaNO<sub>3</sub> (purity no less than  $99\%$ ) was purchased from Fuchen Chemical Reagent Factory, Tianji, China. Concentrated sulphuric acid (purity of  $98\%$ ) was purchased from Chuandong Chemical Group Co. Ltd., Chongqing, China. H<sub>2</sub>O<sub>2</sub> (purity of  $30\%$ ) was purchased from Shandian pharmaceutical Co. Ltd., Kunming, China. MnSO<sub>4</sub>·H<sub>2</sub>O (purity no less than  $99\%$ ) was purchased from Xilong Chemical Factory Co. Ltd., Shantou, China. Deionized water made by the reverse osmosis system was used throughout.

### 2.2 Preparation of MnO<sub>2</sub> and MnO<sub>2</sub>/RGO nanocomposite

The MnO<sub>2</sub> nanorod was prepared by a hydrothermal method with the same procedure as in our previous work.<sup>27</sup> In a typical synthesis, the as-received manganese sulfate mono-hydrate (MnSO<sub>4</sub>·H<sub>2</sub>O,  $1.5$  mmol) and potassium permanganate (KMnO<sub>4</sub>,  $1$  mmol) powders were dissolved in  $40$  ml deionized water successively under strong stirring at room temperature to obtain purple aqueous solution. The resulting solution was transferred into a Teflon lined stainless steel autoclave ( $50$  ml) after magnetically stirring for  $30$  min. The hydrothermal process was carried out at  $180$  °C for  $12$  h. After cooling down to room temperature, the dark products were rinsed with deionized water *via* centrifuge at a rotation rate of  $8000$  rpm for  $3$  times with each time for  $10$  minutes. The obtained powder was dried in a vacuum oven at  $80$  °C for  $12$  hours. The preparation of MnO<sub>2</sub>/RGO composite was similar with above, except the addition GO with a mass ratio of KMnO<sub>4</sub> and GO equaling to  $15 : 1$ . The GO was synthesized from graphite powder through a modified Hummer's method<sup>28</sup> and the corresponding materials used to fabricate GO were also listed in above.

### 2.3 Characterization

X-ray diffraction (XRD) patterns were recorded with a Japan Rigaku TTR-III diffractometer with Cu K $\alpha$  radiation ( $\lambda = 1.5418$  Å) at  $40$  kV and  $200$  mA. The XRD patterns were recorded in the ranges of  $2\theta = 5$ – $80$ °. The XRD specimens were prepared by flattening the powder onto small circular trays whose radius and thickness are  $10$  mm and  $2$  mm, respectively. The Raman spectra was obtained with a Renishaw inVia Raman microscope, equipped with a CCD (charge coupled device) with the detector cooled to about  $153$  K using liquid N<sub>2</sub>. The laser power was set at  $30$  mW and the spectral resolution was  $1$  cm<sup>-1</sup>. Samples were deposited on silicon wafers in powder form without using any solvent. XPS analysis was performed by an X-ray photoelectron spectrometer (Kratos Amicus X-ray photoelectron spectrometer with Al K $\alpha$  radiation). All the binding energies were referenced to the C 1s peak at  $284.8$  eV of the surface adventitious carbon. Scanning electron microscope (SEM) images were obtained using FEI Quanta 200 scanning electron microscopy integrated with energy dispersive X-ray (EDX) from samples obtained by dropping the thick suspension on a silicon slide. Transmission electron microscopy (TEM)

images were obtained using a JEOL JEM-2100 transmittance electron microscopy at 200 kV. The samples for TEM were prepared by dispersing the final sample in the distilled deionized water and then dropped on a copper grid covered by an amorphous carbon film.

The electromagnetic properties of the products were characterized by the complex permittivity and permeability analysis. The products were mixed with paraffin wax in a mass ratio of 1 : 1. To avoid the aggregation of the composites, we first dispersed the composites and paraffin wax into a diethyl ether solution by ultrasonication. The diethyl ether was removed by drying the mixture at 50 °C. The mixtures were then pressed into toroidal-shaped sheets ( $\Phi_{\text{out}} = 7.00$  mm,  $\Phi_{\text{in}} = 3.04$  mm) with thickness of 2 mm. Then the sheet was vertically placed between flange and metal short circuit board and the direction of the microwave was perpendicular to the flat surface of the sheet. The complex permittivity ( $\epsilon_r = \epsilon' - j\epsilon''$ ) and permeability ( $\mu_r = \mu' - j\mu''$ ) of the mixture in the 2–18 GHz frequency range were recorded with coaxial cable method<sup>29–34</sup> using an 2 port models Agilent N5230A vector network analyzer (VNA) with models from 2 GHz up to 18 GHz (the apparatus and the sample are presented in Fig. 11 of the ESI†). The microwave absorbing properties, in terms of microwave reflection loss (RL) were calculated according to the transmission line theory,<sup>35</sup> expressed as follows

$$RL = 20 \log \left| \frac{Z_{\text{in}} - Z_0}{Z_{\text{in}} + Z_0} \right|, Z_{\text{in}} = Z_0 \sqrt{\frac{\mu_r}{\epsilon_r}} \tanh \left[ j \frac{2\pi f d}{c} \sqrt{\mu_r \epsilon_r} \right] \quad (1)$$

where  $f$  is the frequency of microwave,  $d$  is the thickness of the absorbent,  $c$  is the velocity of light,  $Z_0$  and  $Z_{\text{in}}$  are the intrinsic impedance of free space and input impedance of the materials, respectively.  $\epsilon_r$  and  $\mu_r$  represent the relative complex permittivity and permeability, respectively.

### 3. Results and discussion

#### 3.1 Phase crystallinity

The phase and purity of the resulting materials were tested by XRD analysis. For  $\text{MnO}_2$ , all diffraction peaks (Fig. 1(b)) can be indexed to the pure tetragonal phase of  $\beta\text{-MnO}_2$  (JCPDS 24-0735,  $a = b = 4.4$  Å,  $c = 2.874$  Å) with the space group of  $P42/mnm$  (136). From Fig. 1(a), it can be seen that the product obtained with the GO solution mixed into is identified to have two different phases of manganese in the composite which are corresponding to  $\text{MnOOH}$  (JCPDS 41-1379,  $a = 5.3$  Å,  $b = 5.278$  Å,  $c = 5.307$  Å) and  $\alpha\text{-MnO}_2$  (JCPDS 44-0141,  $a = b = 9.785$  Å,  $c = 2.863$  Å). Meanwhile, three other peaks located at 9, 22 and 33° can be indexed to (002), (101), (006) crystal facets of RGO, which is in line with those reports in literature.<sup>36</sup> The broadening diffraction peaks of the composite (Fig. 1(a)) compared with that of the pure manganese dioxide (Fig. 1(b)) indicate that the Mn related phases in the composite has a nanocrystalline essence with poor crystallinity. It can be obviously revealed that the Mn phases in the composite are different to that of pure  $\text{MnO}_2$  sample.

The Raman spectroscopy was also used to further investigate the composition and microstructure of the composite. Raman

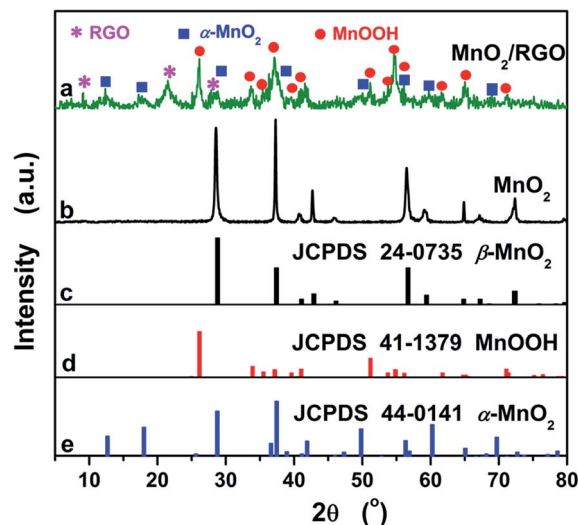


Fig. 1 XRD patterns of  $\text{MnO}_2/\text{RGO}$  nanocomposites and the pure  $\text{MnO}_2$ .

spectroscopy is an effective method to identify carbon materials. As shown in Fig. 2, the Raman spectrum derived from the as-synthesized  $\text{MnO}_2/\text{RGO}$  samples exhibits four peaks in 120–390  $\text{cm}^{-1}$ , which are corresponding to the alpha  $\text{MnO}_2$  type materials. There are three other peaks located at 502, 576, 629.6  $\text{cm}^{-1}$ , which are the characteristic of birnessite type  $\text{MnOOH}$ .<sup>37</sup> The peaks at the 1603 and 1361  $\text{cm}^{-1}$  represent G and D bands, respectively. The G band is the radial C–C stretching mode of  $\text{sp}^2$  bonded carbon, while the D band is a first-order zone boundary phonon mode associated with the defects in the graphene or graphene edge.<sup>38,39</sup> A weak D band indicates a low density of defects and disorder of the graphitized structure. The intensity ratio of D band to G band ( $I_{\text{D}}/I_{\text{G}}$ ) reflects the degree of the defects in the graphene or the edges.<sup>40</sup> A much higher intensity ratio of  $I_{\text{D}}/I_{\text{G}}$  for the  $\text{MnO}_2/\text{RGO}$

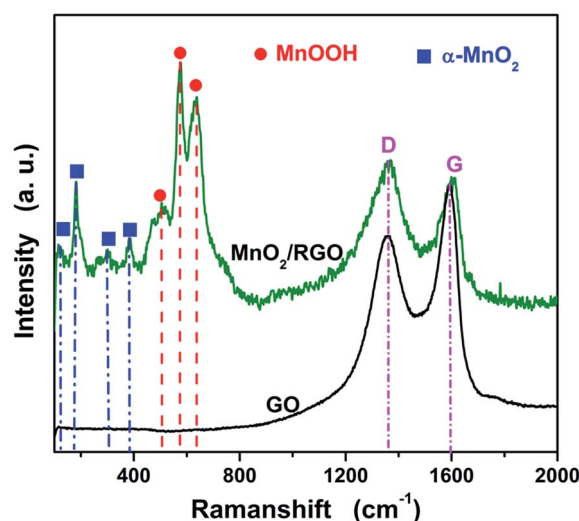


Fig. 2 Raman spectra of  $\text{MnO}_2/\text{RGO}$  nanocomposites and graphene oxide.

composite is achieved than that for graphene oxide, which exhibits the presence of a large amount of carbonic defects. Compared with GO, the G band becomes weaker and broader, suggesting a higher degree of defects in the reduced graphene oxide or the edges due to the reduction in the procedure of hydrothermal synthesis.<sup>41</sup> These defects on the reduced graphene oxide basal plane caused by the adverse excessive restacking of graphene nanosheets could act as polarized centers for the dipole/electrons polarization. Consequently, when the EM field is in the high frequency, the dipole and electrons polarizations could not match up with the changes of EM field, which will lead to the Debye relaxation contributing to enhancing the dielectric loss and electromagnetic energy dissipation.<sup>42</sup> Furthermore, the partly reduction of GO will further increase the material conductivity<sup>43,44</sup> and enhance the microwave absorbing performance.

Fig. 3(a) shows the XPS survey spectra of GO and the MnO<sub>2</sub>/RGO composites. The bands in the wide scan XPS spectra of MnO<sub>2</sub>/RGO confirm the presence of C 1s, O 1s and the Mn 2p. The observed O 1s peak lying in 533.1 eV in GO is shifted to a lower binding energy (531.4 eV) in the composites due to the attachment of the manganese dioxide.<sup>45</sup> The peaks at 642.7 and 654.2 eV (Fig. 3(b)) corresponds to Mn 2p<sub>3/2</sub> and Mn 2p<sub>1/2</sub>,

respectively.<sup>46</sup> The C 1s spectra of GO (Fig. 3(c)) and the MnO<sub>2</sub>/RGO composites (Fig. 3(d)) consist of three main components, arising from C=C/C-C (284.6 eV) in the aromatic rings, C=O/C-O (ranging from 286.4 eV to 287.8 eV) groups and O-C=O (289.3 eV) groups.<sup>47</sup> Compared Fig. 3(c) with Fig. 3(d), the C/O ratio in the composites increases remarkably compared with that of GO, demonstrating that the C-O and C=O functional groups are partly removed in the hydrothermal process. Such a higher C/O ratio of the composite implies much part of GO is reduced and a good electronic conductivity is formed, which can facilitate the graphene sheets to serve as the conductive channels between the manganese oxide phases and is favorable for microwave absorption.<sup>18,19</sup> The indication of the result of the XPS analysis is in a good agreement with what the result of the Raman analysis means.

### 3.2 Characterization of morphologies

The morphologies of the as-prepared pure MnO<sub>2</sub> product were examined by SEM. Fig. 4(a) shows that the pure MnO<sub>2</sub> exhibits a nanorod-like shape with a diameter of *ca.* 100 nm and length of 1.5–2.0 μm as well as a pyramid-like top end of the nanorods. The TEM and HRTEM images of the sample MnO<sub>2</sub> (Fig. 4(b) and inset) further confirm the one-dimensional feature of MnO<sub>2</sub>

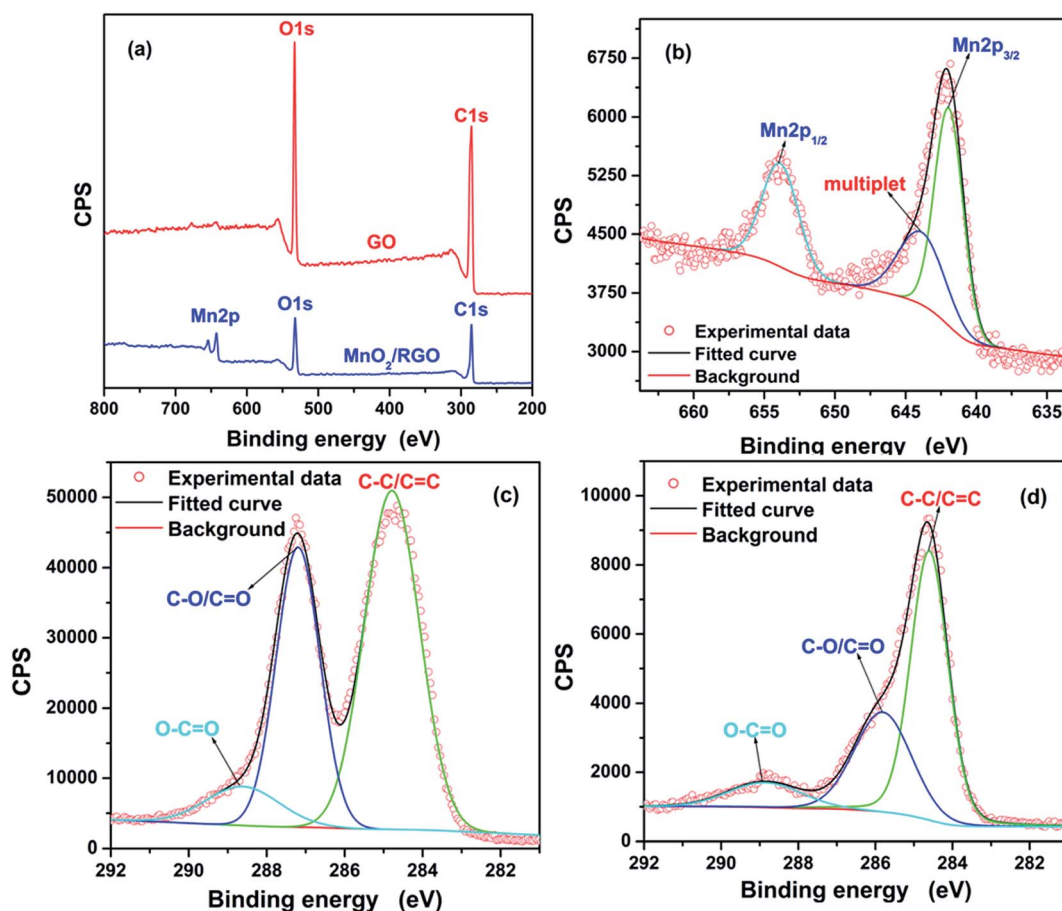


Fig. 3 X-ray photoelectron spectroscopy (XPS) spectra (a) survey curve; (b) Mn 2p spectrum of the MnO<sub>2</sub>/RGO nanocomposites; (c) C 1s spectrum of GO; and (d) C 1s spectrum of MnO<sub>2</sub>/RGO nanocomposites.

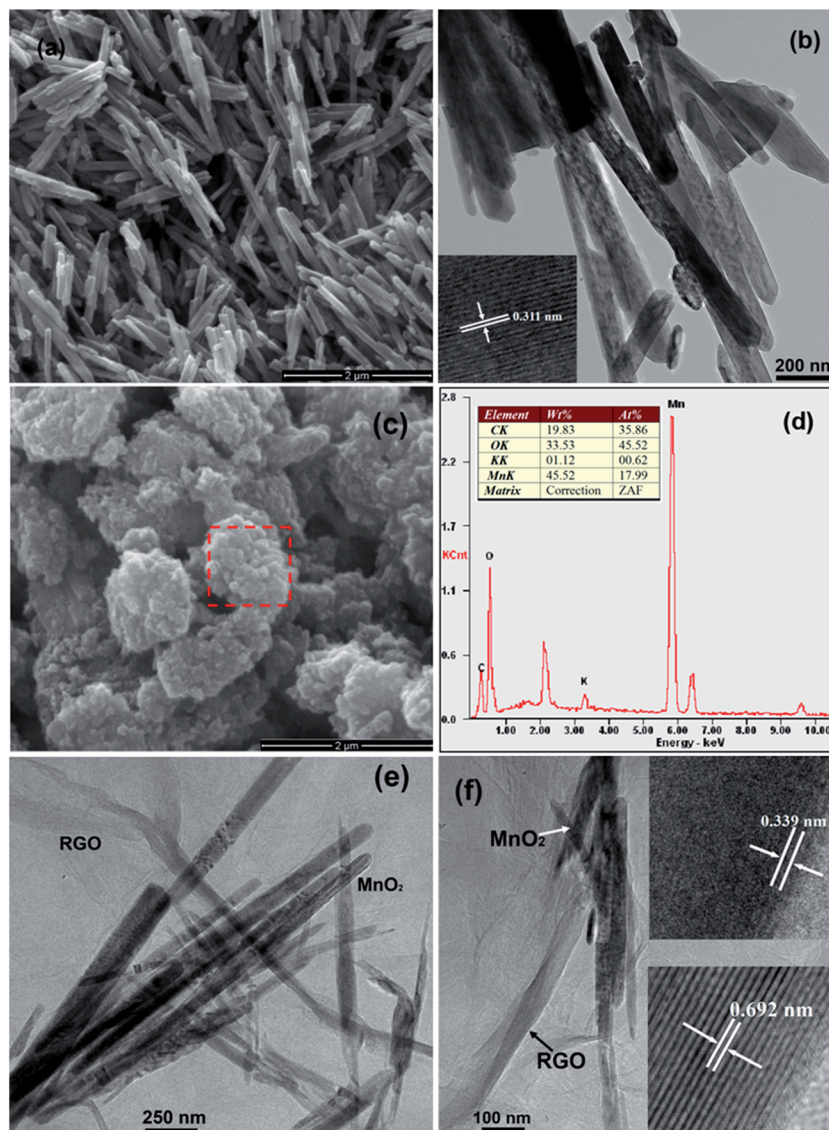


Fig. 4 (a) SEM image of the pure  $\text{MnO}_2$ ; (b) TEM image of the pure  $\text{MnO}_2$  and the inset representing the HR-TEM image; (c) SEM image, (d) EDS spectra, (e) TEM and (f) HR-TEM images of  $\text{MnO}_2/\text{RGO}$  nanocomposites.

nanorods and their higher crystalline degree. HRTEM analysis (inset of Fig. 4(b)) shows the clear lattice fringe with a lattice spacing of 0.3108 nm which corresponds to the interplanar distance of (110) planes. Fig. 4(c) shows the SEM image of the  $\text{MnO}_2/\text{RGO}$  composites displaying that  $\text{MnO}_2$  nanorods are wrapped by the RGO nanosheets on the surface. EDX analysis of the nanocomposites (Fig. 4(d)) indicates that besides manganese (Mn) and oxygen (O) originated from manganese oxide, there are other elements detected such as C and a very small amount of K, which can be related to RGO covering the surface of  $\text{MnO}_2$  and the trapped trace oxygenated potassium permanganate. The morphology and structure of the composite was further investigated by TEM (Fig. 4(e)) and HR-TEM (Fig. 4(f)) analyses. It can be seen that the RGO nanosheets from the reduction in the process of hydrothermal synthesis showing crumpled and rippled structures. Furthermore, RGO nanosheets are well loaded by  $\text{MnO}_2$  nanorods with a diameter of 90–

100 nm. The HR-TEM image shown in Fig. 4(f) also reveals the crystalline structure of  $\text{MnO}_2$  nanorods and the lattice fringes with interplanar distances of 0.339 and 0.692 nm which can be assigned to the (11 $\bar{1}$ ) planes of the monoclinic crystal  $\text{MnOOH}$  and (110) planes of the tetragonal crystal  $\alpha\text{-MnO}_2$ , respectively. These results are consistent with those of XRD analysis showing (Fig. 1).

### 3.3 Electromagnetic properties

The electromagnetic parameters (complex permittivity,  $\epsilon_r = \epsilon' - j\epsilon''$  and complex permeability  $\mu_r = \mu' - j\mu''$ ) and microwave absorbing properties of the samples were investigated in the microwave frequency range of 2–18 GHz at room temperature. As we all know, the real permittivity ( $\epsilon'$ ) and the real permeability ( $\mu'$ ) represent the material abilities to store electric and magnetic energy, while the imaginary permittivity ( $\epsilon''$ ) and the

imaginary permeability ( $\mu''$ ) represent the dissipation of electric and magnetic energy, respectively.<sup>48</sup>

As shown in Fig. 5(a), the  $\epsilon'$  of the MnO<sub>2</sub> nanorods and MnO<sub>2</sub>/RGO nanocomposites in 2–18 GHz are in the range of 5.83–5.60 and 10.28–13.80, respectively, and the  $\epsilon'$  of the MnO<sub>2</sub>/RGO composites is much higher than that of the pure MnO<sub>2</sub> nanorods. Meanwhile, the values of  $\epsilon''$  of the samples MnO<sub>2</sub> and MnO<sub>2</sub>/RGO are in the range of 0.3–1.0 and 1.9–3.2, respectively, and the  $\epsilon''$  of the composites is also much higher than those of the pure MnO<sub>2</sub> nanorods. This suggests that the addition of RGO increases the electric polarization, since  $\epsilon_r$  is an expression of the polarizability of a material, which consists of dipolar polarization and electric polarization at microwave frequency.<sup>19,49</sup> Furthermore, all  $\epsilon'$  show decrease tendency with the increasing frequency, which can be attributed to the phenomenon of dispersion of materials,<sup>50</sup> and can be further confirmed by the famous Debye equation *i.e.*,  $\epsilon' = \epsilon_\infty + (\epsilon_s - \epsilon_\infty)/(1 + \omega^2\tau^2)$  where the decrease in  $\epsilon'$  is attributed to the increase in angular frequency ( $\omega$ ). Fig. 5(b) shows the complex permeability values of both samples. The  $\mu'$  values for both of the two

samples are much similar and have small fluctuation near 1.0 in the whole frequency range of 2–18 GHz. It suggests that dielectric loss properties dominate the microwave absorbing performance of MnO<sub>2</sub>/RGO composite.

To understand the loss properties of incident electromagnetic wave attenuation as a microwave absorbent, the calculated dielectric loss tangent ( $\tan \delta_E = \epsilon''/\epsilon'$ ) and magnetic loss tangent ( $\tan \delta_M = \mu''/\mu'$ ) of the MnO<sub>2</sub> nanorods and MnO<sub>2</sub>/RGO nanocomposites are shown in Fig. 6(a) and (b), respectively. The hybrid of RGO leads to a stronger dielectric loss tangent but a smaller magnetic loss tangent. It shows that in Fig. 6(b), the MnO<sub>2</sub>/RGO nanocomposites and pure MnO<sub>2</sub> nanorods show very weak magnetic loss tangent with the values closely equaling to 0 over the whole frequency range of 2–18 GHz and it also affirms the dominating role of dielectric loss playing in the microwave absorbing performance of MnO<sub>2</sub>/RGO composite.

To make a more clear presentation of microwave absorbing properties of the as-prepared samples, the thickness dependence of absorption peak frequencies and the bandwidth with effective

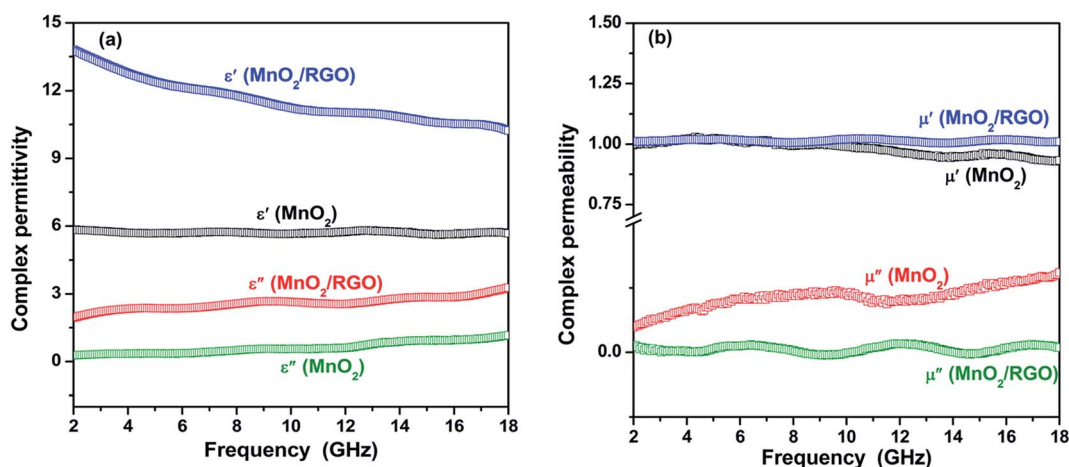


Fig. 5 Complex permittivity (a) and complex permeability (b) of the pure MnO<sub>2</sub> nanorods and MnO<sub>2</sub>/RGO composites, respectively.

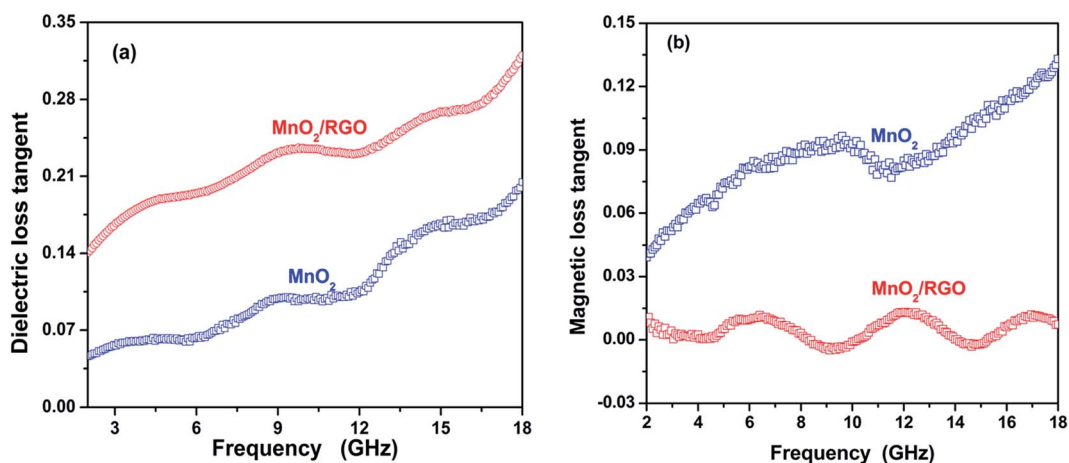


Fig. 6 Dielectric loss (a) and magnetic loss (b) tangents of the pure MnO<sub>2</sub> nanorods and MnO<sub>2</sub>/RGO nanocomposites, respectively.

absorption (RL < -10 and -20 dB) over the frequency of 2–18 GHz are calculated based on the experimentally determined complex permittivity and permeability. The thickness of the sample is one of the major factors affecting both the intensity and position of the reflection loss (RL) peak. Fig. 7 shows the calculated RL of the MnO<sub>2</sub> nanorods and MnO<sub>2</sub>/RGO nanocomposite with different thicknesses. It can be observed that all the absorbing peaks for the two samples become weaker and shift to a lower frequency with the increasing thickness. Generally, when the EM wave is transmitting into the microwave absorption medium, the peak frequency  $f_m$  can be expressed by the quarter-wavelength equation model which is expressed as  $t = nc/(4f\sqrt{\epsilon_r\mu_r})(n = 1, 3, 5, \dots)$ .<sup>51</sup> In this equation,  $t$  is the thickness of sample,  $\epsilon_r$  and  $\mu_r$  are the complex permittivity and permeability at the corresponding frequency. It indicates that the thickness is inversely related to the frequency, which just demonstrates the phenomenon shown in Fig. 7. Based on the quarter-wavelength ( $\lambda/4$ ) model, it is found that the matching peak frequency and thickness of both materials can be precisely figured out. The figure that we compared simulated matching

thicknesses ( $t_m^{\text{sim}}$ ,  $n$  equals 3 and 5) and frequencies according to the quarter-wavelength equation model to the results ( $t_m^{\text{cal}}$ ) calculated based on the transmission line theory is presented in Fig. 8. Besides, from Fig. 7, it can be seen that the MnO<sub>2</sub>/RGO composites show much stronger wave-absorbing abilities than the pure MnO<sub>2</sub> nanorods with the same thickness. The maximum reflection loss value reaches -37 dB at 16.8 GHz with a thickness of 2.0 mm. Furthermore, At the same time, the effective absorption bandwidth, with the reflection loss below -10 dB, of the composite is much wider than that of the pure MnO<sub>2</sub> nanorods with the same thickness. It starts from 13 GHz until a value of -22 dB at 18 GHz.

To further understand the reflection loss mechanism, the microwave amplitude attenuation coefficient ( $\alpha$ ) is proposed as follows:

$$\alpha = \frac{\pi f}{c} (\epsilon' \mu')^{1/2} \left\{ \left[ \tan \delta_E \tan \delta_M - 1 + (1 + \tan^2 \delta_E + \tan^2 \delta_M + \tan^2 \delta_E \tan^2 \delta_M)^{1/2} \right] \right\}^{1/2} \quad (2)$$

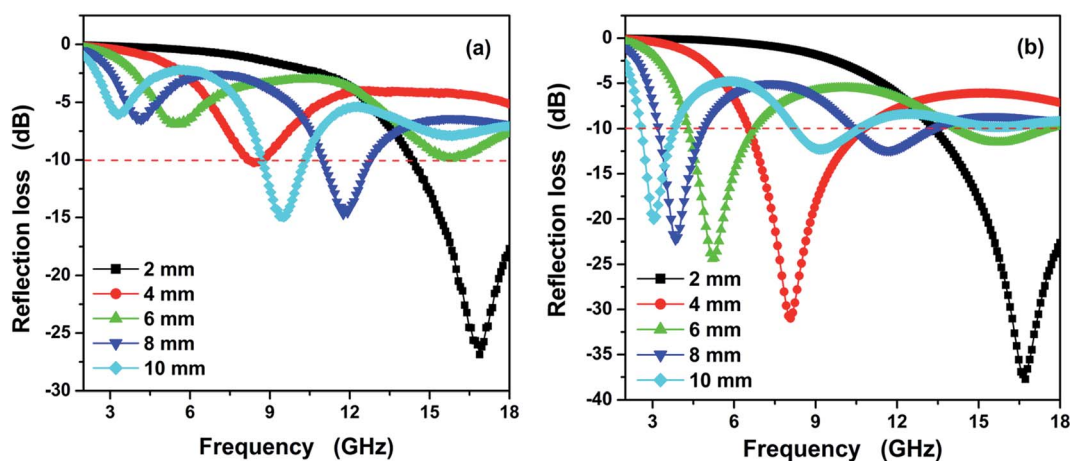


Fig. 7 Reflection loss of the pure MnO<sub>2</sub> nanorods (a) and MnO<sub>2</sub>/RGO nanocomposites (b), respectively.

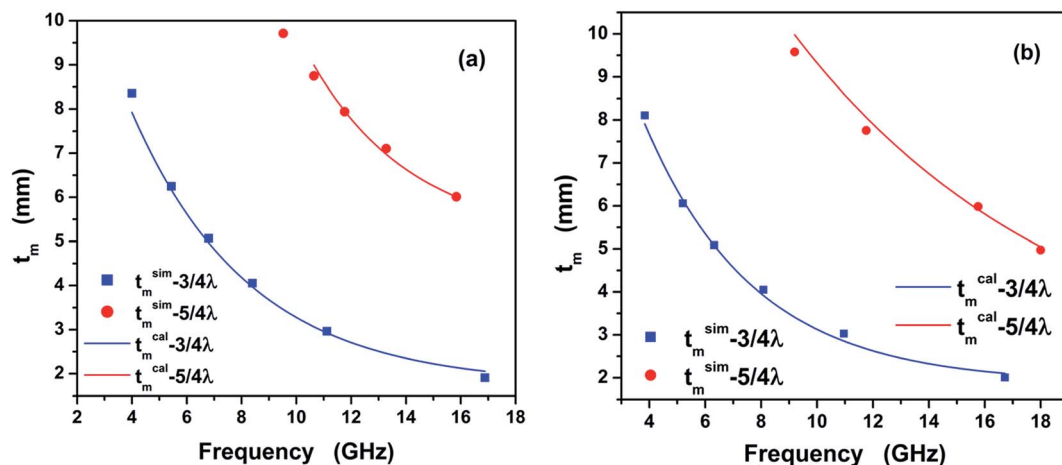


Fig. 8 Dependence of  $3\lambda/4$  and  $5\lambda/4$  thickness on frequency for the pure MnO<sub>2</sub> nanorods (a) and MnO<sub>2</sub>/RGO nanocomposites (b).

where  $f$  is the frequency of the electromagnetic wave ping on the samples and  $c$  is the velocity of light which equals to  $3 \times 10^8$  m s<sup>-1</sup>. The EM wave multiple attenuation coefficient ( $\alpha$ ) is calculated by the measured  $\epsilon'$  and  $\mu'$  and its variation *versus* the frequency is shown in Fig. 9. The multiple EM attenuation coefficients of the two samples all raise with the increasing of frequency, which is consistent to the tendency of imaginary permittivity. It gives a clear clue pointing to the important effect of dielectric properties on the microwave absorbing performance. Besides, the  $\alpha$  of the MnO<sub>2</sub>/RGO nanocomposite is much higher than that of the pure MnO<sub>2</sub> nanorods, which just can explain why the reflection loss property of the nanocomposite is superior to the pure MnO<sub>2</sub> nanorods with the same thickness.

So far, there are few groups who have ever explored the microwave absorbing properties and mechanisms of MnO<sub>2</sub>/RGO composites. As far as concerned, the introduction of RGO

significantly enhanced the properties of loss tangent and microwave absorption. In light of EM theory, there are several factors that lead to this phenomenon. The first reason is the domain factor that caused by improving the dielectric loss capability of the MnO<sub>2</sub>/RGO nanocomposites. As confirmed by the Raman spectrum analysis, the residual defects on the reduced graphene oxide basal plane caused by the adverse excessive restacking of graphene nanosheets and the interface between the MnO<sub>2</sub> nanorods and the RGO nanosheets could act as polarized centers for the dipole/electrons polarization. Consequently, when the EM field is in the high frequency, the dipole and electrons polarizations could not match up with the changes of EM field, which will lead to the Debye relaxation contributing to enhancing the dielectric loss and electromagnetic energy dissipation.<sup>42</sup> Secondly, the existence of complex phases in MnO<sub>2</sub>/RGO composites and the unique micro structures of birnessite type MnOOH as well as the  $\alpha$ -MnO<sub>2</sub> with the tunnel structure of  $2 \times 2$  facilitate the transportation of electron, which are beneficial to enhance dipole polarization and contribute to the dielectric loss and microwave absorbing properties. In addition, the large aspect ratio and unique layered structure of the RGO nanosheets is another reason for the better absorbing abilities. Furthermore, according to the free electron theory,  $\epsilon'' = 1/2\epsilon_0\pi\rho f$ , where  $\epsilon_0$  is the permittivity in vacuum,  $\rho$  is the material conductivity,  $f$  is the radiation frequency, the high conductivity of RGO enables a higher  $\epsilon''$  of the nanocomposites than that of the pure MnO<sub>2</sub> nanorods, finally leading to an increase in the dielectric loss. Above all, the synergetic effect of manganese dioxide and reduced graphene oxide contributes to the improved microwave attenuation properties of nanocomposite.

In order to clearly explain the microwave response properties and microwave attenuation, we adopt the Debye dielectric relaxation model (Cole–Cole model) to further interpret the mechanisms of the dielectric loss. The real permittivity and imaginary permittivity are expressed as follows,

$$\epsilon' = \epsilon_\infty + \frac{\epsilon_s - \epsilon_\infty}{1 + \omega^2\tau^2} \quad (3)$$

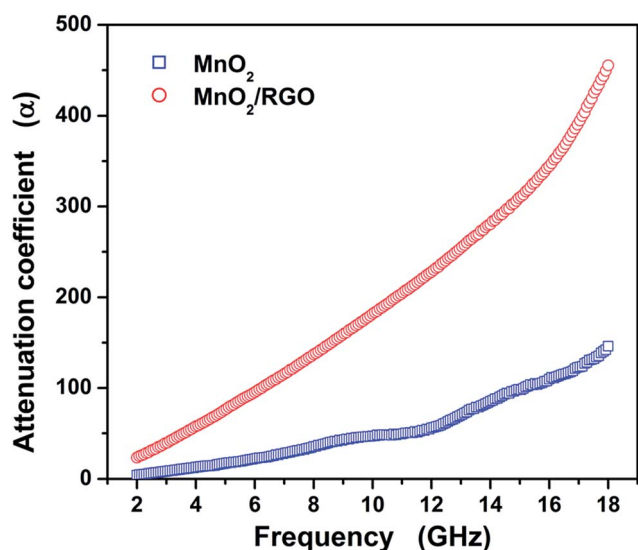


Fig. 9 Amplitude attenuation factors of the pure MnO<sub>2</sub> nanorods and MnO<sub>2</sub>/RGO nanocomposites *versus* radiation frequency.

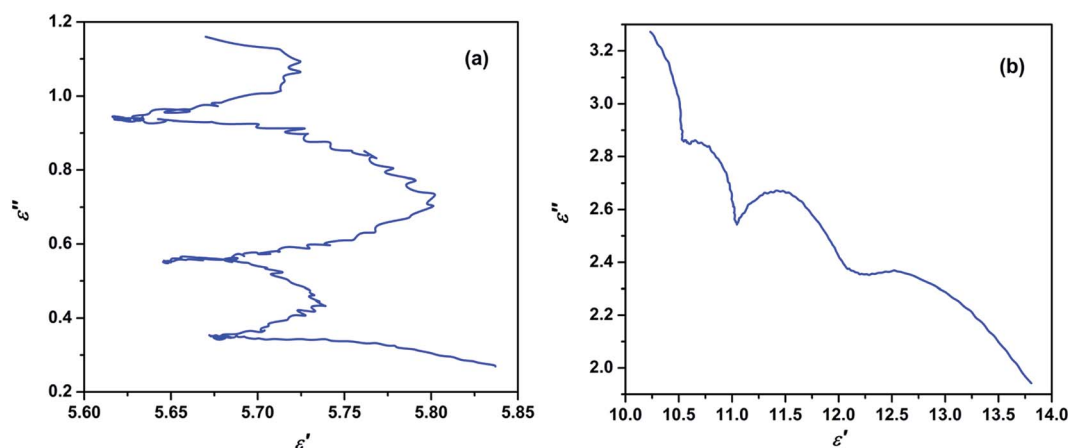


Fig. 10 Cole–Cole plots for the pure MnO<sub>2</sub> nanorods (a) and MnO<sub>2</sub>/RGO nanocomposites (b).

$$\varepsilon'' = \frac{\varepsilon_s - \varepsilon_\infty}{1 + \omega^2 \tau^2} \omega \tau + \frac{\sigma}{\omega \varepsilon_0} \quad (4)$$

According to eqn (3) and (4), the relationship between  $\varepsilon'$  and  $\varepsilon''$  can be deduced as

$$\left(\varepsilon' - \frac{\varepsilon_s + \varepsilon_\infty}{2}\right)^2 + (\varepsilon'')^2 = \left(\frac{\varepsilon_s - \varepsilon_\infty}{2}\right)^2 \quad (5)$$

Thus, the plot of  $\varepsilon'$  versus  $\varepsilon''$  is a single semicircle, generally denoted as the Cole–Cole semicircle.<sup>52</sup> Each semicircle corresponds to one Debye relaxation process. Fig. 10(a) and (b) show the  $\varepsilon''$  versus  $\varepsilon'$  curves for the both samples. As shown, there are various relaxation processes existed. Apparently, the Cole–Cole semicircles of the samples are distorted, suggesting that there are other kinds of dissipation besides the dielectric relaxation. Such as conductance loss caused by the improvement of conductivity of the composites, interfacial polarization relaxation resulted from the combination interface of the composites as well as defects in the composites can increase the space polarization and improve the dielectric dissipation, which give rise to the enhanced EMW absorption properties.<sup>53</sup>

## 4. Conclusions

In summary, the MnO<sub>2</sub> nanorods/RGO nanosheet composites with an obviously enhanced microwave absorption property have been successfully synthesized by a one-step hydrothermal method which avoided the usage of any toxic reduced agent. The results show that the manganese dioxide nanorods are very well dispersed on the surface of the RGO nanosheets. The MnO<sub>2</sub> nanorods–RGO nanosheets composites extraordinarily improved the electromagnetic absorption performance in comparison with the pure MnO<sub>2</sub> nanorods, which is attributed to the excellent dielectric loss properties of nanocomposites. The dielectric loss of the composites can be attributed to Debye dipolar relaxation, electron polarization relaxation, interfacial polarization and the unique microstructure facilitated for transport of electrons in the nanocomposites. It is believed that MnO<sub>2</sub> nanorods–reduced graphene oxide nanocomposites can be used as an effective microwave absorbent and the implication of fundamental understanding and mechanism gained here can provide potential strategies for designing high performance EM wave absorbing materials. Moreover, it is considered that the research in electromagnetic absorption properties of MnO<sub>2</sub> nanorods–reduced graphene oxide nanocomposites can provide a new perspective for semiconductor material of wide band gap being used in the field of electromagnetic.

## Acknowledgements

This work was supported by the National Natural Science Foundation of China (Grant No. 51262029), the Application Basic Research Fund of Yunnan Province (Grant No.

2013FB006), and Yunnan University Graduate Program for Research and Innovation (Grant No. YNUY201452).

## Notes and references

- D. D. L. Chung, *Carbon*, 2001, **39**, 279–285.
- J. Xiao, H. F. Zhang, Y. Xue, Z. W. Liu, X. Q. Chen, P. Su, F. J. Yang and X. B. Zeng, *Ceram. Int.*, 2015, **41**, 1087–1092.
- D. D. L. Chung, *Carbon*, 2012, **50**, 3342–3353.
- Y. L. Yang and M. C. Gupta, *Nano Lett.*, 2005, **5**, 2131–2134.
- M. H. Al-Saleh and U. Sundararaj, *Carbon*, 2009, **47**, 1738–1746.
- N. Li, Y. Huang, F. Du, X. B. He, X. Lin, H. J. Gao, Y. F. Ma, F. F. Li and Y. S. Chen, *Nano Lett.*, 2006, **6**, 1141–1145.
- W. L. Song, M. S. Cao, B. B. Qiao, Z. L. Hou, M. M. Lu, C. Y. Wang, J. Yuan, D. N. Liu and L. Z. Fan, *Mater. Res. Bull.*, 2014, **51**, 277–286.
- S. H. Park, P. Thielemann, P. Asbeck and P. R. Bandaru, *Appl. Phys. Lett.*, 2009, **94**, 243111.
- F. J. Ren, H. J. Yu, L. Wang, M. Saleem, Z. F. Tian and P. F. Ren, *RSC Adv.*, 2014, **28**, 14419–14431.
- R. C. Che, L. M. Peng, X. F. Duan, Q. Chen and X. L. Liang, *Adv. Mater.*, 2004, **16**, 401–405.
- W. K. Hsu, A. Barnes and B. Chambers, *Chem. Phys. Lett.*, 2003, **378**, 609–614.
- P. C. P. Watts, W. K. Hsu, A. Barnes and B. Chambers, *Adv. Mater.*, 2003, **15**, 600–603.
- Y. C. Du, W. W. Liu, R. Qiang, Y. Wang, X. J. Han, J. Ma and P. Xu, *ACS Appl. Mater. Interfaces*, 2014, **6**, 12997–13006.
- J. T. Han, B. J. Kim, B. G. Kim, J. S. Kim, B. H. Jeong, S. Y. Jeong, H. J. Jeong, J. H. Cho and G. W. Lee, *ACS Nano*, 2011, **5**, 8884–8891.
- Z. F. Liu, G. Bai, Y. Huang, Y. F. Ma, F. Du, F. F. Li, T. Y. Guo and Y. S. Chen, *Carbon*, 2007, **45**, 821–827.
- G. Z. Wang, Z. Gao, S. W. Tang, C. Q. Chen, F. F. Duan, S. C. Zhao, S. W. Lin, Y. H. Feng, L. Zhou and Y. Qin, *ACS Nano*, 2012, **6**, 11009–11017.
- Y. Wang, M. Jaiswal, M. Lin, S. Saha, B. Ozyilmaz and K. P. Loh, *ACS Nano*, 2012, **6**, 1018–1025.
- H. Zhang, A. J. Xie, C. P. Wang, H. S. Wang, Y. H. Shen and X. Y. Tian, *J. Mater. Chem. A*, 2013, **1**, 8547–8552.
- M. Zong, Y. Huang, Y. Zhao, X. Sun, C. H. Qu, D. D. Luo and J. B. Zheng, *RSC Adv.*, 2013, **3**, 23638–23648.
- X. J. Zhang, G. S. Wang, W. Q. Cao, Y. Z. Wei, J. F. Liang, L. Guo and M. S. Cao, *ACS Appl. Mater. Interfaces*, 2014, **6**, 7471–7478.
- M. H. Huang, S. Mao, H. Ferick, H. Q. Yan, Y. Y. Wu, R. Russo and P. D. Yang, *Science*, 2001, **292**, 1897–1899.
- A. R. Armstrong and P. G. Bruce, *Nature*, 1996, **381**, 499–500.
- B. B. Amundsen and J. Paulsen, *Adv. Mater.*, 2001, **13**, 943–966.
- Y. P. Duan, J. Zhang, H. Jing and S. H. Liu, *J. Solid State Chem.*, 2011, **184**, 1165–1171.
- H. T. Guan, Y. Wang, C. J. Dong, G. Chen, X. C. Xiao and Y. D. Wang, *Ceram. Int.*, 2015, **41**, 5688–5695.
- X. X. Wang, J. H. Yu, H. Z. Dong, M. X. Yu, B. Q. Zhang, W. Wang and L. F. Dong, *Appl. Phys. A*, 2015, **119**, 1483–1490.

- 27 H. T. Guan, G. Chen, J. Zhu and Y. D. Wang, *J. Alloys Compd.*, 2010, **507**, 126–132.
- 28 D. C. Marcano, D. V. Kosynkin, J. M. Berlin, A. Sinitskii, Z. Z. Sun, A. Slesarev, L. B. Alemany, W. Lu and J. M. Tour, *ACS Nano*, 2010, **4**, 4806–4814.
- 29 X. J. Zhang, G. S. Wang, W. Q. Cao, Y. Z. Wei, M. S. Cao and L. Guo, *RSC Adv.*, 2014, **4**, 19594–19601.
- 30 M. H. Cao, H. Q. Lian and C. W. Hu, *Nanoscale*, 2010, **2**, 2619–2623.
- 31 H. L. Lv, G. B. Ji, X. H. Liang, H. Q. Zhang and Y. W. Du, *J. Mater. Chem. C*, 2015, **3**, 5056–5064.
- 32 B. Zhao, G. Shao, B. B. Fan, W. Y. Zhao, Y. J. Xie and R. Zhang, *Phys. Chem. Chem. Phys.*, 2015, **17**, 8802–8810.
- 33 M. Najim, G. Modi, Y. K. Mishra, R. Adelung, D. Singh and V. Agarwala, *Phys. Chem. Chem. Phys.*, 2015, **17**, 22923–22933.
- 34 H. Sözeri, Z. Mehmedi, H. Kavas and A. Baykal, *Ceram. Int.*, 2015, **41**, 9602–9609.
- 35 Y. Naito and K. Suetake, *IEEE Trans. Microwave Theory Tech.*, 1971, **19**, 65–72.
- 36 L. L. Peng, X. Peng, B. R. Liu, C. Z. Wu, Y. Xie and G. H. Yu, *Nano Lett.*, 2013, **13**, 2151–2157.
- 37 A. Ogata, S. Komaba, R. B. Hadjean, J. P. P. Ramos and N. Kumagai, *Electrochim. Acta*, 2008, **53**, 3084–3089.
- 38 V. Chandra, J. Park, Y. Chun, J. W. Lee, I. C. Hwang and K. S. Kim, *ACS Nano*, 2010, **4**, 3979–3986.
- 39 Y. Z. Xue, B. Wu, L. Jiang, Y. L. Guo, L. P. Huang, J. Y. Chen, J. H. Tan, D. C. Geng, B. R. Luo, W. P. Hu, G. Yu and Y. Q. Liu, *J. Am. Chem. Soc.*, 2012, **134**, 11060–11063.
- 40 H. L. Guo, X. F. Wang, Q. Y. Qian, F. B. Wang and X. H. Xia, *ACS Nano*, 2009, **3**, 2653–2659.
- 41 J. F. Shen, B. Yan, T. Li, Y. Long, N. Li and M. X. Ye, *Soft Matter*, 2012, **8**, 1831–1836.
- 42 B. Wen, X. X. Wang, W. Q. Cao, H. L. Shi, M. M. Lu, G. Wang, H. B. Jin, W. Z. Wang, J. Yuan and M. S. Cao, *Nanoscale*, 2014, **6**, 5754–5761.
- 43 J. W. Qin, M. H. Cao, N. Li and C. W. Hu, *J. Mater. Chem.*, 2011, **21**, 17167–17174.
- 44 G. H. Yu, L. B. Hu, N. Liu, H. L. Wang, M. Vosgueritchian, Y. Yang, Y. Cui and Z. N. Bao, *Nano Lett.*, 2011, **11**, 4438–4442.
- 45 A. Prakash, S. Chandra and D. Bahadur, *Carbon*, 2012, **50**, 4209–4219.
- 46 C. L. Yu, G. Li, L. F. Wei, Q. Z. Fan, Q. Shu and J. C. Yu, *Catal. Today*, 2014, **224**, 154–162.
- 47 P. B. Liu, Y. Huang and L. Wang, *Mater. Lett.*, 2013, **91**, 125–128.
- 48 M. Zong, Y. Huang, Y. Zhao, X. Sun, C. H. Qu, D. D. Luo and J. B. Zheng, *RSC Adv.*, 2013, **3**, 23638–23648.
- 49 B. P. Rao and K. H. Rao, *J. Mater. Sci.*, 1997, **32**, 6049–6054.
- 50 X. F. Zhang, P. F. Guan and X. L. Dong, *Appl. Phys. Lett.*, 2010, **96**, 223111.
- 51 B. C. Wang, J. Q. Wei, Y. Yang, T. Wang and F. S. Li, *J. Magn. Mater.*, 2011, **323**, 1101–1103.
- 52 K. S. Cole and R. H. Cole, *J. Chem. Phys.*, 1941, **9**, 341–351.
- 53 T. K. Gupta, B. P. Singh, V. N. Singh, S. Teotia, A. P. Singh, I. Elizabeth, S. R. Dhakate, S. K. Dhawan and R. B. Mathur, *J. Mater. Chem. A*, 2014, **2**, 4256–4263.